

“Body Wave Attenuation Heralds Incoming Eruption at Mount Etna”**ATTENUATION TOMOGRAPHY: METHOD**

The attenuation tomography is divided into two main steps (Roth et al., 1999; Rietbrock, 2001; Eberhart-Phillips and Chadwick, 2002): the determination of t^* in the frequency domain from the inversion of the P-wave spectrum, and the inversion of t^* data for the estimation of 3D Q models.

In the first step, t^* is obtained modeling the far-field velocity spectrum. According to Scherbaum (1990), the logarithm of the far-field velocity spectrum of a body wave $V(f)$ is expressed by:

$$\log_{10} V(f) = \log_{10}(2\pi f \Omega_0) + \log_{10} \left[\frac{(f_c)^\gamma}{(f_c)^\gamma + (f)^\gamma} \right] - (\log_{10} e) \pi f t^* (1-\alpha) \quad (1)$$

where f_c is the corner frequency; Ω_0 is the low frequency level depending on the seismic moment; γ is the spectral fall-off, t^* is the operator which quantifies the attenuation along a ray path and α quantifies the dependency of Q_p from frequency.

In our study we used short-period vertical velocity seismograms (seismometer eigenfrequency of 1 Hz), at a sampling frequency of 100 Hz. Assuming a point like source, a ω^{-2} type source model (setting $\gamma=2$ in [1]) and a frequency independent attenuation (setting $\alpha=0$ in [1]) within the 1-30 Hz frequency band, we solved (1) by a damped least squares inversion, using all the P-wave velocity spectra of each event to compute a common event f_c , and single station Ω_0 and t^* . Spectra were computed by using a FFT on a 1.28 s time window following the P wave arrival, with a taper width of 5 %. A Hanning window is used to smooth the spectrum. The same procedure is used to estimate the spectral content of the noise preceding the P-onset. For a spectrum to be fitted, a continuous frequency band ranging from 1 Hz to 15 Hz must be at least 1.3 times greater than the noise spectrum. Since we are interested in estimating the high frequency decay rate, the upper frequency limit is extended to the anti-aliasing frequency (30 Hz) if the signal to noise ratio is above the threshold.

For N spectra recorded for a generic event, we construct the kernel matrix of the inverse problem taking the derivative of equation (1) with respect to each of the unknown parameters: Ω_0 , t^* and f_c . The number of rows of the kernel matrix is the sum of the spectral points of the N spectra of the event while the number of columns is $2N + 1$. We assume that for the i^{th} spectrum the $((i*2)-1)$ and the $(i*2)$ columns are filled with the derivatives of equation (1) with respect to station Ω_0 and t^* ,

respectively. The column N is for the derivative of equation (1) with respect to the corner frequency. All the spectra contribute to the computation of f_c hence, in the kernel matrix, the elements of the column N are not null. For example, if an event has 3 spectra and each spectrum contains 3 points, the inversion scheme is constructed as follows:

$$\begin{bmatrix} RES_{S1P1} \\ RES_{S1P2} \\ RES_{S1P3} \\ RES_{S2P1} \\ RES_{S2P2} \\ RES_{S2P3} \\ RES_{S3P1} \\ RES_{S3P2} \\ RES_{S3P3} \\ \vdots \end{bmatrix} = \begin{bmatrix} \left(\frac{\partial}{\partial \Omega_o}\right)_{S1P1} & \left(\frac{\partial}{\partial t^*}\right)_{S1P1} & 0 & 0 & 0 & 0 & \left(\frac{\partial}{\partial f_c}\right)_{S1P1} \\ \left(\frac{\partial}{\partial \Omega_o}\right)_{S1P2} & \left(\frac{\partial}{\partial t^*}\right)_{S1P2} & 0 & 0 & 0 & 0 & \left(\frac{\partial}{\partial f_c}\right)_{S1P2} \\ \left(\frac{\partial}{\partial \Omega_o}\right)_{S1P3} & \left(\frac{\partial}{\partial t^*}\right)_{S1P3} & 0 & 0 & 0 & 0 & \left(\frac{\partial}{\partial f_c}\right)_{S1P3} \\ 0 & 0 & \left(\frac{\partial}{\partial \Omega_o}\right)_{S2P1} & \left(\frac{\partial}{\partial t^*}\right)_{S2P1} & 0 & 0 & \left(\frac{\partial}{\partial f_c}\right)_{S2P1} \\ 0 & 0 & \left(\frac{\partial}{\partial \Omega_o}\right)_{S2P2} & \left(\frac{\partial}{\partial t^*}\right)_{S2P2} & 0 & 0 & \left(\frac{\partial}{\partial f_c}\right)_{S2P2} \\ 0 & 0 & \left(\frac{\partial}{\partial \Omega_o}\right)_{S2P3} & \left(\frac{\partial}{\partial t^*}\right)_{S2P3} & 0 & 0 & \left(\frac{\partial}{\partial f_c}\right)_{S2P3} \\ 0 & 0 & 0 & 0 & \left(\frac{\partial}{\partial \Omega_o}\right)_{S3P1} & \left(\frac{\partial}{\partial t^*}\right)_{S3P1} & \left(\frac{\partial}{\partial f_c}\right)_{S3P1} \\ 0 & 0 & 0 & 0 & \left(\frac{\partial}{\partial \Omega_o}\right)_{S3P2} & \left(\frac{\partial}{\partial t^*}\right)_{S3P2} & \left(\frac{\partial}{\partial f_c}\right)_{S3P2} \\ 0 & 0 & 0 & 0 & \left(\frac{\partial}{\partial \Omega_o}\right)_{S3P3} & \left(\frac{\partial}{\partial t^*}\right)_{S3P3} & \left(\frac{\partial}{\partial f_c}\right)_{S3P3} \\ \vdots & \vdots & \vdots & \vdots & \vdots & \vdots & \vdots \end{bmatrix} \cdot \begin{bmatrix} (\Delta \Omega_o)_{S1} \\ (\Delta t^*)_{S1} \\ (\Delta \Omega_o)_{S2} \\ (\Delta t^*)_{S2} \\ (\Delta \Omega_o)_{S3} \\ (\Delta t^*)_{S3} \\ (\Delta f_c) \end{bmatrix} \quad (2)$$

where:

RES is the data vector, i.e. the residuals between the observed and computed amplitudes on the basis of the starting values of the unknown parameters (see below); $(\partial/\partial \Omega_o)$, $(\partial/\partial t^*)$, $(\partial/\partial f_c)$ are the partial derivative of (1) with respect to single station Ω_o , t^* and event f_c , respectively;

$\Delta \Omega_o$, Δt^* are the correction to the starting parameters for each spectrum (S_i) while Δf_c is correction for the event corner frequency.

In the kernel matrix, the subscript index $S_i P_j$ indicates the point j-th for the i-th spectrum.

Using the residuals between the observed and computed amplitudes, for each iteration step, the model is computed by a damping least squares scheme and the starting model is updated. The damping parameter is varied to improve the stability of the solution while minimizing the number of iterations.

For one event, the initial guess of the unknown parameters are selected as follows:

- a) the event corner frequency is chosen after the visual inspection of all the spectra;
- b) for each spectrum, the low frequency level Ω_0 is computed using the spectral amplitudes below the selected f_c ;
- c) the starting t^* is computed by the ratio between the known 3D traveltime (Patanè et al., 2002; Patanè et al., 2006) and a starting Q_P of 100, as mean value for the structure of Mt. Etna down to 10-12 km depth (De Gori et al., 2005).

In the iterative fitting procedure, a maximum of 20 iterations are allowed. However, the majority of adjustments occur in the first 3-5 iterations and the RMS reduction varies, for a single event, from 40 to 80 %.

All the t^* computed are weighted on the basis of the goodness of the spectral fit. The RMS between the observed and computed amplitudes are translated into a weight to be used in the tomographic inversion of t^* . Following Eberhart-Phillips and Chadwick (2002), we assign weights of 0, 1, 2, 3 or 4 for RMS less than 0.1, 0.2, 0.3, 0.4 respectively. As commonly adopted for the quality of the phase picks, 0 is the best observation while 4 is associated to the worst, and is skipped for Q tomography. An example of fitting Ω_0 , t^* and f_c for one event is shown in Fig. DR1.

The tomographic inversion for Q_P structure relies on the definition of t^* that can be expressed as a line integral along the ray-path:

$$t^* = \int_{ray} \frac{ds}{V(ds)Q(ds)} + (t^*)_{site} \quad (3)$$

where $V(r)$ and $Q(r)$ are the velocity and quality factor for the P-wave along the segment of raypath with length ds . The term $(t^*)_{site}$ quantifies the shallow attenuation near the seismic station. Starting from a priori locations and 3D velocity model, t^* depends only on the Q values along the rays.

The t^* have been inverted for the 3D Q_P structure and $(t^*)_{site}$ by using the code developed by Thurber (1993) and modified for attenuation by Rietbrock (2001). For the three epochs, the medium is parameterized with the same 3D grid of nodes (in the central part of the model, nodes are spaced 2 km by 2 km by 1 km) and velocity values reported in Patanè et al. (2002, 2006), assuming an initial Q_P equal to 75. A damping of 0.003 s is added to the diagonal elements of the inverted matrix to optimize the model complexity and residual variance trade off (Eberhart-Phillips, 1986). Table DR1 summarizes the data used and statistics for the three inversions. The values of station $(t^*)_{site}$ are within ± 0.01 s. Comparing these values with t^*

deriving from spectral fitting, we estimate that $(t^*)_{\text{site}}$ are on average less than 10-15 % of the t^* along the complete ray-path.

SOURCE MODEL AND FREQUENCY DEPENDENCY OF Q_p

Following the literature, in the fitting procedure we assume: i) a point like source, ii) a frequency independent attenuation, and iii) a ω^{-2} type source model.

i) The point source approximation is justified by the low magnitude of the events (more than 90% of them have magnitude < 3.0). For such small earthquakes, rupture directivity and spectral effects related to the finite length of the fault can be neglected (Haberland and Rietbrock, 2001).

ii) In general, the dependence of Q on frequency is described by the power law $Q=Q_0f^\alpha$, where Q_0 is the frequency independent Q . At Mt. Etna, Giampiccolo et al. (2007) found that Q_p is weakly frequency-dependent in the central part of the volcano. Attenuation tomography studies reveal that the pattern of Q_p anomalies is similar and equivalent whether or not the frequency dependence is considered (Rietbrock, 2001; Eberhart-Phillips et al., 2008). In order to verify how this assumption influences the results, we run a test varying α between 0 and 1, with the step of 0.1, and fitting all the velocity spectra (Rietbrock, 2001). In addition, we used two different source models, ω^{-2} and ω^{-3} ($\gamma=2$ and $\gamma=3$ in equation 1) to explore the third assumption discussed below. Fig. DR2 shows the overall RMS of spectral fit versus α values, for the two considered source models. We find a similar RMS fit for α ranging between 0 and 0.5, in agreement with the weak frequency-dependency of Q_p recognized by Giampiccolo et al. (2007), justifying the choice of using $\alpha = 0$.

iii) The source model influences the spectral fall off at frequencies higher than f_c . Thus, the assumption of the source model leads to a different estimate of the absolute value of t^* . In all the recent attenuation tomography studies, a ω^{-2} model is adopted (Rietbrock, 2001; Eberhart-Phillips and Chadwich, 2002; Haberland and Rietbrock, 2001; De Gori et al., 2005). In the test described above, we observe that the ω^{-2} source model fits the observed spectra better with α lower than 0.5, in agreement with observations from other attenuation studies (Rietbrock, 2001; Eberhart-Phillips and Chadwich, 2002; Haberland and Rietbrock, 2001; Hawksson and Shearer, 2006).

In summary, the assumption of a different source model, or a frequency dependent Q_p , would only influence the absolute values of Q_p and not the 3D anomaly pattern.

It is noteworthy that the Ω_0 and f_c values obtained by our inversion are consistent with seismic moments and stress drops observed at Mount Etna (Giampiccolo et al., 2007; Patanè et al., 1994, 1997), reinforcing the validity of our approach. In particular, the estimated seismic moments for the eruptive periods are within the range $10^{13} - 10^{15}$ Nm, stress drop values are between 0.1 and 10 MPa, with source radius between 0.1 and 1 km.

ATTENUATION TOMOGRAPHY: MODEL RESOLUTION AND SYNTHETIC TESTS

The reliability of tomography images has been verified by the analysis of the full-resolution matrix (Toomey and Foulger, 1989), computing and visualizing the matrix diagonal elements, the averaging vectors (rows of the matrix) and the spread function (SF, i.e., the dispersion of each row of the matrix (Michellini and McEvilly, 1991; De Gori et al., 2005)). A perfectly resolved node has a delta-like averaging vector, and values on the respective row of the matrix strongly peaked on the diagonal element, i.e. large diagonal element, negligible off-diagonal elements resulting in a small value of SF. In order to visualize the directions of anomaly smearing, we contour the volume where the resolution is 70% of the diagonal element (Eberhart-Phillips and Chadwick, 2002). Well-resolved nodes have low values of SF and smearing effects localized in the surrounding nodes. The best resolved parameters of our three models are characterized by $SF \leq 2.0$, and are located beneath the central-eastern part of the volcano between -1 and 2 km depth (Fig. DR3).

In addition, we run two synthetic tests to assess the capability of recovering a transient Q_p anomaly during the 2002-2003 eruption by differential tomography and t^* changes. We compute the difference between the Q_p tomographic model of 2002-2003 eruption and that one relative to the pre-eruptive period. In particular, we use synthetic anomalies that are similar to those obtained in the real data inversions but of opposite sign. For the 2002-2003 pre-eruptive period the synthetic model consists of a low Q_p anomaly ($Q_p=25$) located in the central part of volcano, between -1 and 1 km depth. The same geometry is used for the eruptive 2002-2003 period, where a high Q_p anomaly is used ($Q_p=125$). For each synthetic model, t^* are computed by forward modeling. Random white noise equal to 10% of the mean t^* computed for all the observations is added to synthetic data. The high noise level accounts for the uncertainties in the computation of the t^* operators. The inversions are carried out as in the real case. The differential model (eruptive minus pre-eruptive model) shows that the synthetic transient anomaly is recovered above 50 % between -1 to 1 km depth (Fig. DR4).

In the test for the t^* time-changes, we use synthetic anomalies that reproduce the low Q_p bodies imaged by the tomographic models. To simulate the intruding dykes, synthetic low Q_p bodies ($Q_p=25$) are located beneath the central summit area during the 2001 and 2002-2003 eruptions, using the same geometry as in figure DR4. In the intra eruptive period, the Q_p model is unperturbed. Synthetic t^* and random noise are computed as in the synthetic test described above. Successively, t^* are converted in Q_p using the traveltimes in the 3D velocity models. The average Q_p is computed for each event and a moving window is used to produce the final trend using the same procedure described for the time-changes in the main text. The comparison between the retrieved time-series and those computed with the real data (see Fig. 3 of the main

text) demonstrates that this qualitative approach is highly reliable.

REFERENCES

- De Gori, P., Chiarabba, C., and Patanè D., 2005, Q_P structure of Mount Etna: constraints for the physics of the plumbing system: *J. Geophys. Res.*, v. 110, B05303, doi: 10.1029/2003JB002875.
- Eberhart-Phillips, D., 1986, Three dimensional velocity structure in Northern California Coast Ranges from inversion of local earthquake arrival times: *Bull. Seismol. Soc. Am.*, v. 76, p. 1025-1052.
- Eberhart-Phillips, D., and Chadwick, M., 2002, Three-dimensional attenuation model of the shallow Hikurangi subduction zone in the Raukumara peninsula, New Zealand: *J. Geophys. Res.* v. 107(B2), 2033, doi: 10.1029/2000JB000046.
- Eberhart-Phillips, D., Reyners, M., Chadwick, M., and Stuart, G., 2008, Three-dimensional attenuation structure of the Hikurangi subduction zone in the central North Island, New Zealand: *Geophys. J. Int.*, v. 174, p. 418–434, 10.1111/j.1365-246X.2008.03816.
- Giampiccolo, E., D'amico, S., Patanè, D., Gresta, S., 2007, Attenuation and source parameters of shallow microearthquakes at Mt. Etna volcano: *Bull. Seism. Soc. Am.*, v. 97(1B), p. 184-197.
- Haberland, C., and Rietbrock, A., 2001, Attenuation tomography in the western central Andes: a detailed insight into the structure of a magmatic arc: *J. Geophys. Res.*, v. 106, p. 11,151 –11,167.
- Hawksos, E., and Shearer, P.M., 2006, Attenuation models (Q_P and Q_S) in three dimensions of the southern California crust: inferred fluids saturation a seismogenic depth: *J. Geophys. Res.*, 111(B05302), 10.1029/2005JB003947.
- Michelson, A., and McEvilly, T.V., 1991, Seismological studies at Parkfields I: Simultaneous inversions for velocity structure and hypocenters using a cubic B-splines parameterization: *Bull. Seism. Soc. Am.*, v. 81, p. 524-552.
- Patanè, D., Barberi, G., Cocina, O., De Gori, P., and Chiarabba, C., 2006, Time-resolved seismic tomography detects magma intrusions at Mount Etna: *Science*, v. 313, p. 821-823.
- Patanè, D., Chiarabba, C., Cocina, O., De Gori, P., Moretti, M., and Boschi, E., 2002, Tomographic images and 3D earthquake locations of the seismic swarm preceding the 2001 Mt. Etna eruption: Evidence for a dyke intrusion: *Geophys. Res. Lett.*, v. 29 (10), 1497, doi:10.1029/2001GL014391.
- Patanè, D., Ferrucci, F., Giampiccolo, E., Scaramuzzino, L., 1997, Source scaling of microearthquakes at Mt. Etna volcano and in the Calabrian Arc (southern Italy): *Geophys. Res. Lett.*, 24, 1879–1882.
- Patanè, D., Ferrucci, F., Gresta, S., 1994, Spectral features of microearthquakes in volcanic areas: attenuation in the crust and amplitude response of the site at Mt. Etna, Italy: *Bull. Seism. Soc. Am.*, v. 84, p. 1842-1860.

- Rietbrock, A., 2001, P wave attenuation structure in the fault area of the 1995 Kobe earthquake. *J. Geophys. Res.*, v. 106, p. 4141– 4154.
- Roth, E.G., Wiens, L.M., Dorman, J., Hildebrand S.C., and Webb, S.C., 1999, Seismic attenuation tomography of the Tonga-Fiji region using phase pair methods: *J. Geophys. Res.*, v. 104, p. 4795-4809.
- Scherbaum, F., 1990, Combined inversion for the three-dimensional Q structure and source parameters using microearthquake spectra: *J. Geophys. Res.*, v. 95, p. 12423-12438.
- Thurber, C. H., 1993, Local earthquake tomography: velocity and Vp/Vs theory, in Iyer, H., and Hirahara, K., eds., *Seismic Tomography: Theory and Practice*: Boca Raton, Fla, CRC Press, p. 563– 580.
- Toomey, D. R., Foulger, G.R., 1989, Tomographic inversion of local earthquake data from the Hengill-Grensdalur central volcano complex, Iceland: *J. Geophys. Res.*, v. 94, p. 17497-17510.

FIGURESCAPTIONS

Figure DR1. Examples of P-wave spectra. The red line corresponds to the portion of the spectrum used to calculate the fit (thick black line). The noise spectrum is also shown as the black dotted line. For each spectrum the vertical bar indicates the corner frequency, common to all the stations of the event. Furthermore, $t^* Q$ and W is the weight used in the tomographic inversion, calculated using the RMS between observed and computed spectral amplitudes

Figure DR2. Overall RMS of spectral fit versus α values, for the two considered source models ($\gamma=2$ and $\gamma=3$ in equation 1).

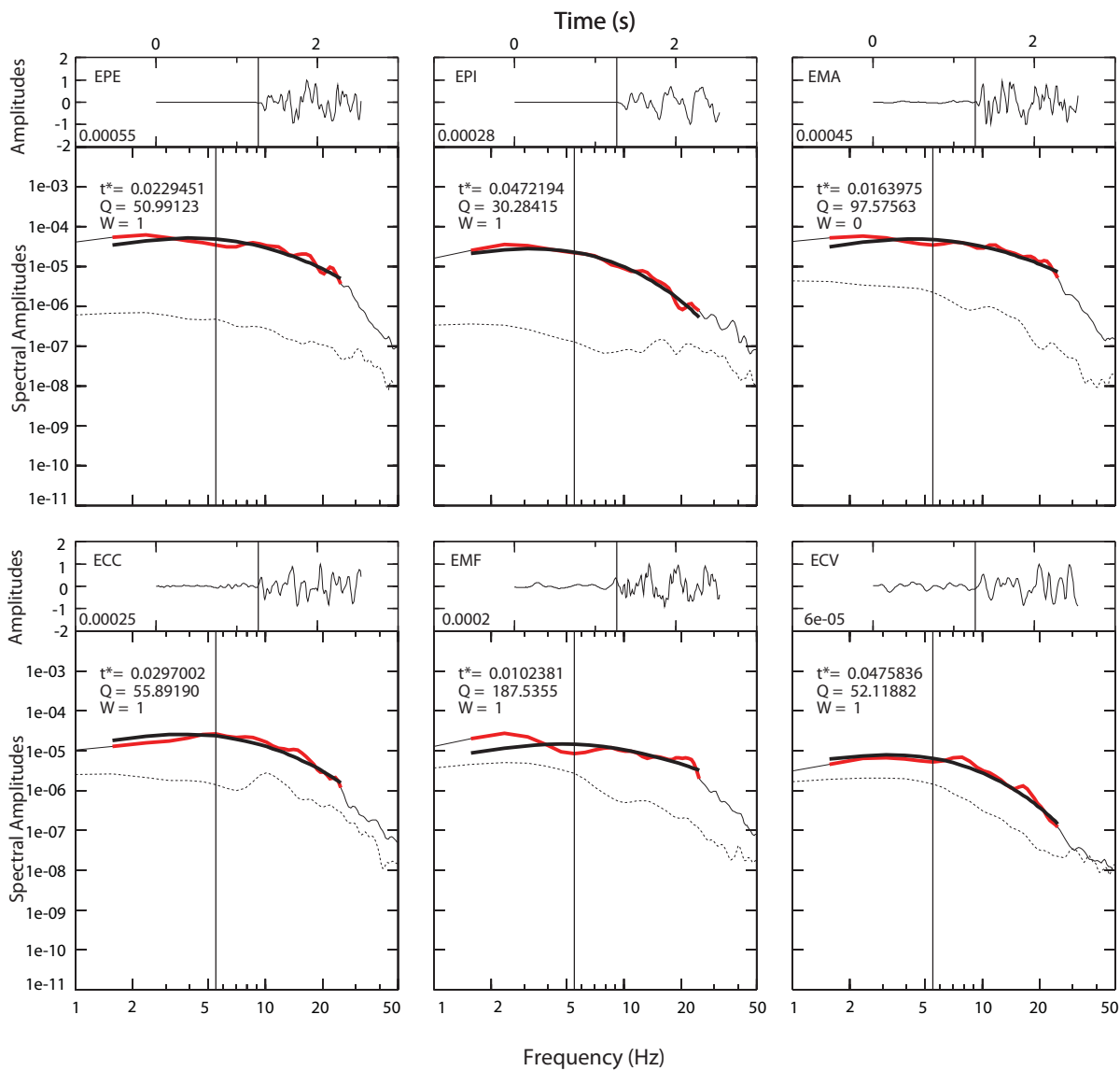
Figure DR3. 70 % smearing contour for nodes with spread function (SF) < 1.5 (black) and with $1.5 < SF < 2.0$ (grey) in the three Q_P models. The red box from -1 to 1 km depth indicates the region where the main temporal variations are detected (see the main text Fig. 2 and Fig. 4).

Figure DR4. Synthetic test on transient Q_P anomalies. Left) Synthetic model for the 2002-2003 eruption period. It consists of a high Q_P body ($Q_P = 125$) located beneath the central part of volcano, from -1 to 1 km depth. During the pre-eruptive period, the synthetic model consists of a low Q_P body ($Q_P = 25$) with the same spatial distribution. Right) Differential tomographic model obtained by subtracting the pre-eruptive model from the eruptive one. The anomalies are expressed as percentage of the starting differential anomaly. The thin black line represents the region where the resolution is satisfactory in both the models ($SF \leq 2$).

Figure DR5. Moving average of Q_P vs. time, since 1 July 2001, as obtained by the synthetic test for the whole 2001-2003 period (a), and local zoom on the 2001 (b), and 2002-2003 (c) eruptive periods. Synthetic Q_P time-series are obtained with a low Q_P intruding dykes placed in the volcano axis during the 2001 and 2002-2003 eruptions.

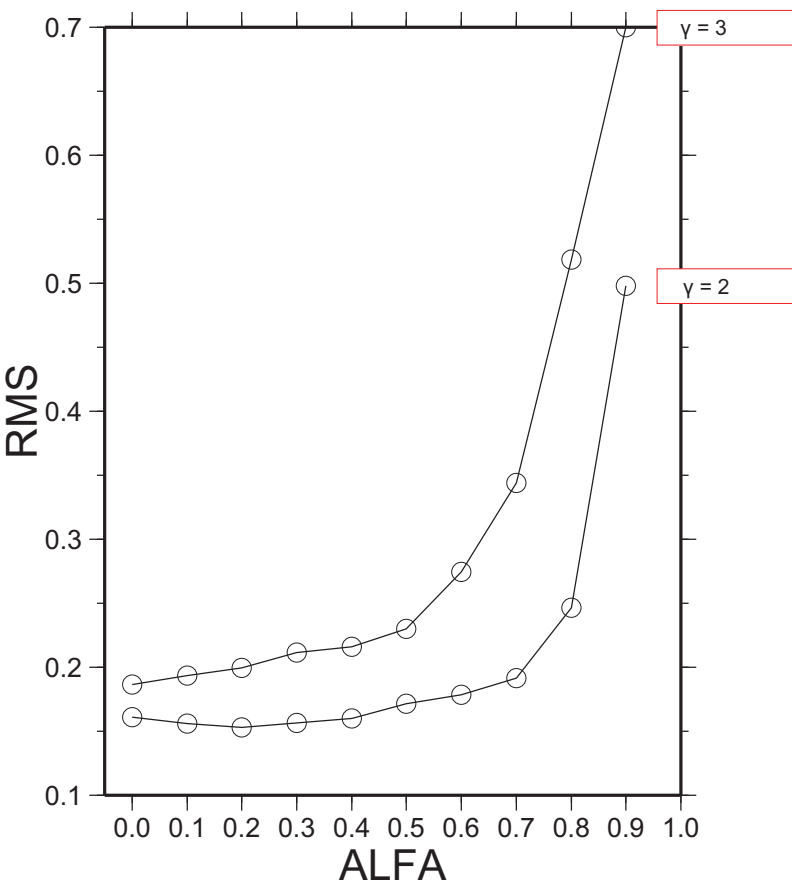
TABLE DR1. SUMMARY OF THE INVERTED PARAMETERS FOR EACH DATASET .

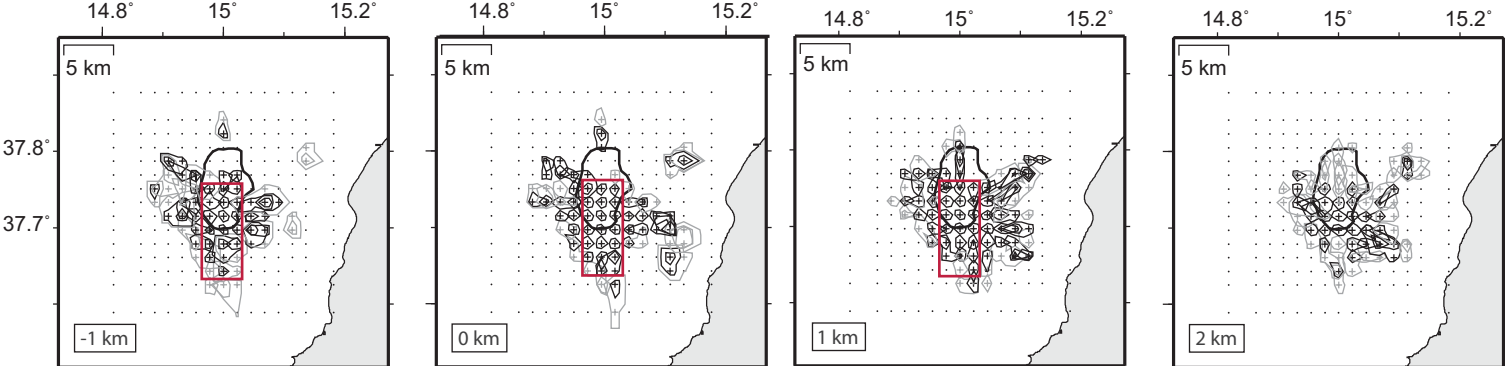
	2001 eruption	2002-2003	2002-2003 eruption
Number of events	232	212	185
Number of t^*	2442	1929	2190
Final RMS	0.0140	0.0126	0.01261
Variance improvement (%)	38	55	40



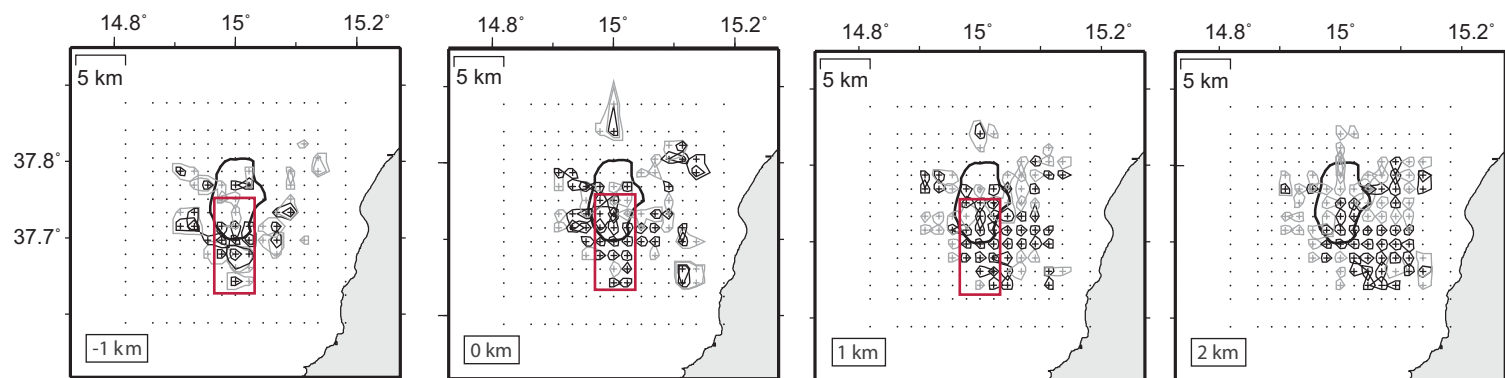
DR Fig.01

RMS Vs ALFA

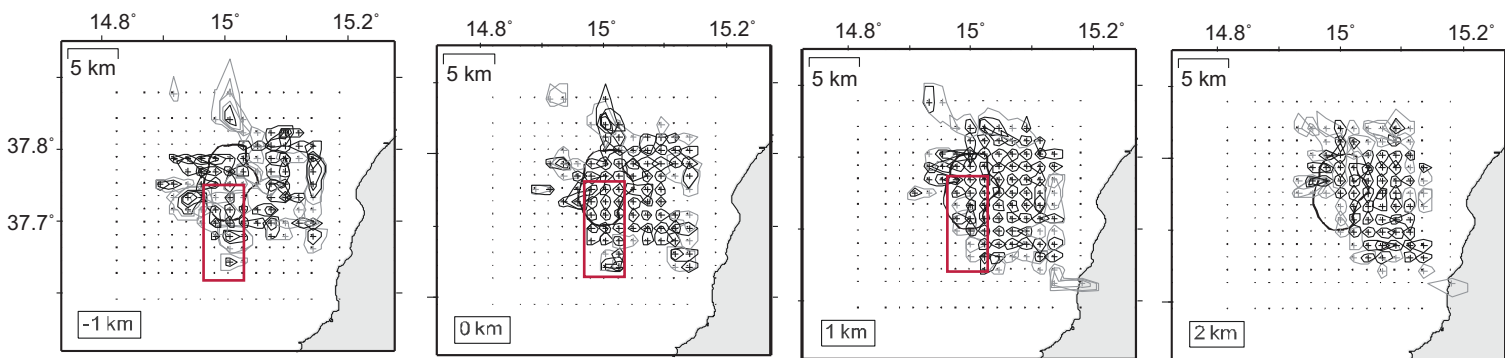




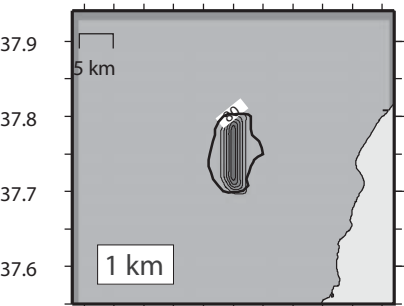
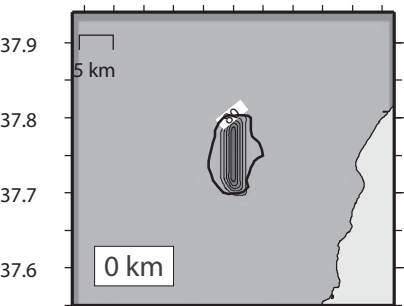
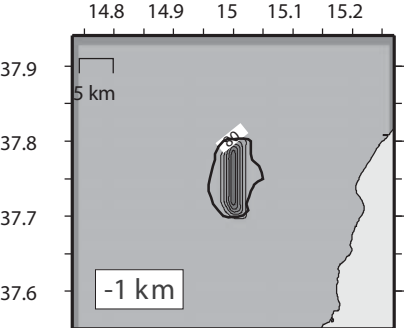
2001 Eruption



2001 - 2002 pre-eruptive period



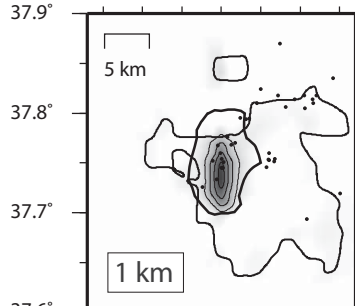
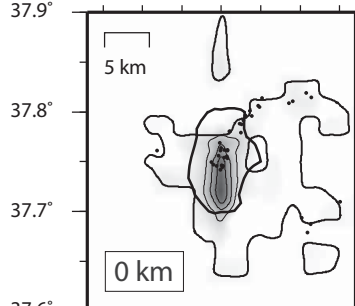
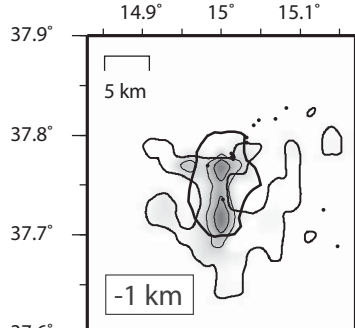
2002-2003 Eruption



50 100 150

Q_p

synthetic anomaly
($Q_p=125$ during 2002-2003
eruption)



0 50 100

Recovered DQ_p (%)
difference between
2002-2003 eruptive ($Q_p=125$)
and pre-eruptive periods ($Q_p=25$)

